



Full length article

Toughness enhancement in TiN/WN superlattice thin films

Julian Buchinger^{a,*}, Nikola Koutná^a, Zhuo Chen^b, Zaoli Zhang^b, Paul Heinz Mayrhofer^a, David Holec^c, Matthias Bartosik^a

^a Institute of Materials Science and Technology, TU Wien, Getreidemarkt 9, Vienna, A-1060, Austria

^b Erich Schmid Institute of Materials Science, Austrian Academy of Sciences, Jahnstraße 12, Leoben, A-8700, Austria

^c Department of Materials Science, Montanuniversität Leoben, Leoben, A-8700, Austria

ARTICLE INFO

Article history:

Received 11 February 2019

Received in revised form

10 April 2019

Accepted 13 April 2019

Available online 17 April 2019

Keywords:

Superlattice

Fracture toughness

Thin film

Sputtering

DFT

ABSTRACT

Transition metal nitride thin films traditionally possess a low intrinsic fracture toughness. Motivated by the recently discovered fracture toughness enhancing superlattice (SL) effect, as well as the remarkably high potential for toughness predicted by theoretical studies for TiN/WN superlattices, we synthesise a series of these materials by DC reactive magnetron sputtering. The SL coatings demonstrate a vacancy-stabilised cubic configuration throughout, as well as a marginal lattice mismatch between the TiN and WN layers. All investigated mechanical properties produced a distinct dependence on the bilayer period, featuring a hardness peak of 36.7 ± 0.2 GPa and a minimum of the indentation modulus of 387 ± 2 GPa. The toughness-related quantities of the SLs in particular show a significant enhancement compared to monolithic TiN and WN, including a tripling of the fracture energy. The fracture toughness is raised from 2.8 ± 0.1 (TiN) and 3.1 ± 0.1 (WN) to 4.6 ± 0.2 MPa \sqrt{m} by the SL arrangement. We relate this maximisation to the vastly disparate elastic moduli and compositional fluctuations. To complement our experimental data, we present Density Functional Theory-based models to disentangle the conspicuous trends observed for TiN/WN superlattices.

© 2019 Acta Materialia Inc. Published by Elsevier Ltd. This is an open access article under the CC BY license (<http://creativecommons.org/licenses/by/4.0/>).

1. Introduction

The superlattice (SL) structure – which is characterised by ultrathin layers of two alternately and coherently grown materials – has been demonstrated to be an effective approach to simultaneously enhance the hardness and the fracture toughness of hard protective coatings. Within the field of nitride based SLs, a pioneering experimental study by Helmersson et al. [1] revealed that the hardness of TiN/VN SLs with a bilayer period of 5.2 nm is more than doubled compared to monolithic TiN and VN, as well as ternary TiVN [1]. Building upon this finding, Chu and Barnett conceived a model to describe the superlattice effect based on dislocation glide within the layers and across the interfaces in these systems [2]. The claim that the difference in shear modulus between the individual layers constitutes the main reason for the hardness maximum was strengthened most prominently by studies on the TiN/Nb_xV_{1-x}N system [3]. Mirkarimi, Hultman and Barnett [3] selected a composition x of Nb_xV_{1-x}N that matched TiN in terms

of its lattice parameter, but retained a disparate shear modulus to isolate the effect of coherency strains and shear moduli on the hardness enhancement. Although the coherency strains between the layers were virtually nullified, the authors observed a hardness maximum at a bilayer period of about 8.2 nm.

More recently, investigations on TiN/CrN SLs suggested that the superlattice effect also extends onto the fracture toughness [4]. By employing in-situ micromechanical cantilever bending tests on freestanding superlattice films, the authors found that the fracture toughness increased with decreasing bilayer period (Λ), reaching a maximum at $\Lambda \sim 6$ nm. For ultrathin layers ($\Lambda \sim 2$ nm), the fracture toughness dropped to the lowest value. Since the recorded load-displacement data in the micromechanical tests suggested pure elastic deformation until failure, it was concluded that other bilayer-period dependent mechanisms than those identified by Chu and Barnett [2] must be responsible for the peak in fracture toughness. These might be: coherency strains, misfit dislocation arrays at the interface, spatially oscillating elastic moduli influencing crack growth, average grain size and other defects confined into individual layers.

The potential of SLs to increase the toughness of transition metal nitrides (TMNs) also elicited a surge of interest from the realm of

* Corresponding author.

E-mail address: julian.buchinger@tuwien.ac.at (J. Buchinger).

theoretical studies. Employing Density Functional Theory (DFT), Wang et al. calculated semi-empirical indicators for the fracture toughness of numerous nitride-based superlattice-like systems, albeit only for structures featuring TiN as one of the two constituents [5]. They identified the TiN/WN system as the most auspicious candidate, as it shows a remarkably high B/G ratio and a highly positive Cauchy pressure [5]. However, the bilayer period of their model is as thin as 2 atomic layers, and therefore insufficiently large for precise comparison with our experimental work. Despite their promising performance in simulations, TiN/WN superlattices are far from trivial in practice, largely due to the complexity of the WN system. Under ambient conditions WN crystallises in a hexagonal close-packed (hcp) arrangement [6]. Additionally, numerous vacancy-stabilised polymorphs of the cubic NaCl-based WN_x have been proposed in the literature. Despite showing the lowest formation energy at 0 K, the NbO-type phase (space group Pm-3m) with 25% of vacancies on both sublattices [7,8] is seldom reported in experimental studies [9]. Unlike that, the solely N vacancies featuring rs- WN_x has been successfully synthesised for a wide range of stoichiometries, showing that the occupation of the N sublattice depends strongly on the applied deposition conditions [10,11]. Vacancies in general, can effectively influence the preferred crystal structure as well as metastable solubility limits of such systems, as shown for Ta-Al-N [12], Mo-Al-N [13], and Mo-Cr-N [14].

While the current state of research may present the hardness-maximising SL effect as a thoroughly studied topic, the fracture toughness of such structures has only been explored by a singular experimental observation thus far. Hence, the aim of the present study is to expand on this initial finding. TiN/WN is a predestined system for this purpose. The extraordinary performance of TiN-WN-related structures in terms of the criteria proposed by Pugh and Pettifor [5,15] in combination with the considerable difference between the elastic constants of TiN [16] and WN [8,17] as well as the possibility to manipulate the lattice parameter of WN via the vacancy concentration should render the resulting enhancement of the fracture toughness particularly pronounced and informative.

The present study is roughly divided into three parts. In the first part, we show and discuss theoretical results produced by DFT, in order to obtain an overview of the expected properties of the involved material systems, as well as to assess the theoretical feasibility of the project. We then use this knowledge to tailor our experimental approach, the results of which are presented in the central section, including dissections of XRD, nanoindentation, fracture toughness and morphological data. To further our understanding of the observed relationships in the experiment we present one final theoretical section on the mechanical properties of TiN/WN SLs. Whenever appropriate, we let theory and experiment coalesce to gain a more holistic perspective.

2. Methodology

2.1. Modelling

The Vienna Ab-initio Simulation Package (VASP) [18,19] together with the projector augmented plane wave (PAW) pseudopotentials were employed to carry out the Density Functional Theory (DFT) calculations. The exchange-correlation effects were treated under the generalised gradient approximation (GGA) [20] using a Perdew-Burke-Ernzerhof (PBE) exchange and correlation functional [21]. The plane-wave cut-off energy was always set to 600 eV, while the k-vector sampling of the Brillouin zone provided a total energy accuracy of about 10^{-3} eV/at. or better. Our simulation cells were based on the cubic rocksalt (Fm-3m) structure. In particular, stacking a desired number of cubic cells in the (100)

direction produced TiN/WN SLs with various bilayer periods. Vacancies in both the bulk and the SL systems were distributed in an ordered (e.g., the NbO-type WN) or disordered manner employing the Special Quasirandom Structure (SQS) method [22]. In the latter case, a sufficiently large supercell (containing 64 and 128 atoms for the bulk and the SL systems, respectively) was constructed. Lattice parameters of the defect-free structures were optimised by fitting the energy vs. volume data with the Birch-Murnaghan equation of state [23] while all structure optimisations in the vacancy-containing variants were performed by relaxing supercell volumes, shapes, and atomic positions.

Chemical stability of various systems was quantified by calculating their formation energy, E_f ,

$$E_f = \frac{1}{\sum_s n_s} \left(E_{\text{tot}} - \sum_s n_s \mu_s \right) \quad (1)$$

wherein E_{tot} represents the total energy of the supercell, n_s and μ_s correspond to the number of atoms and the chemical potential, respectively, of a species s . The reference chemical potentials for Ti, W, and N are conventionally chosen to be the total energy per atom of hcp-Ti, bcc-W, and the N_2 molecule, respectively.

Dynamical stability, assured by an absence of soft phonon modes in vibrational spectra, was investigated for selected systems using the Phonopy package [24]. To assess elastic properties of various structural candidates, a tensor of elastic constants was calculated from the Hooke's law by applying the stress-strain method [25–27]. Subsequently, we used the Voigt's notation to transform this fourth-order elastic tensor to a 6×6 matrix, which was further projected onto a desirable (cubic or tetragonal) symmetry [28]. The polycrystalline bulk, B, and shear, G, moduli were determined by averaging the Reuss' and Voigt's estimates [29,30], while the polycrystalline Young's modulus, E, was evaluated as $E = 9BG/(3B + G)$, which is valid for isotropic systems. Following the formulae in Ref. [31] we computed Young's modulus values in the prominent crystallographic directions.

Tendencies for brittle/ductile behaviour were reviewed by plotting the B/G ratio vs. Cauchy pressure, $c_{12}-c_{44}$ [15]. In the case of NaCl-based TiN/WN SLs - which do not exhibit overall cubic but tetragonal symmetry - effective Cauchy pressure values were estimated as $1/3(c_{12}-c_{66} + c_{13}-c_{55} + c_{23}-c_{44})$. Since bilayer period dependent trends in mechanical properties are very costly to obtain from first-principles (especially for defected systems), we adapted the linear elasticity continuum model by Grimsditch and Nizzoli [32] to calculate effective elastic constants of SLs composed of two layers with arbitrary symmetries. In the original formalism, the algorithm requires elastic constants of the two-layer materials together with their volumetric ratio, disregarding any heterogeneity introduced by interfaces. In particular, the input elastic constants correspond to the equilibrium lattice parameters of each individual phase, which improperly represent the stress state of the material in the SL. To incorporate a more realistic picture of the interface, we extended the formalism to SL composed of n-layer materials. The interface-related effects were entered by setting the elastic constants of one of the involved layer materials to those of chosen superlattice, SL^* , with a bilayer period Λ^* . At $\Lambda = \Lambda^*$ the volumetric ratio of SL^* was 100%, while an increase of (the total) Λ gradually diminished the interface effects by decreasing the volume ratio of SL^* to incorporate more of the "bulk-like" layers.

Moreover, to corroborate our fracture experiments, tensile strength in terms of cleavage energy and stress for brittle cleavage were estimated using the rigid-block displacement method [33,34].

2.2. Experimental procedures

All coatings – both superlattices and monolithic films – investigated in this work were synthesised via unbalanced DC reactive magnetron sputtering using an AJA International Orion 5 magnetron sputtering deposition system. We mounted one 3" Ti target and one 2" W target onto the respective cathodes and used the computer-controlled shutter system to synthesise SL coatings with bilayer periods between 2.8 and 166.7 nm. Si (100) and MgO (100) substrates were ultrasonically cleaned first in acetone and then in ethanol for 5 min and subsequently mounted in a rotatable substrate holder. Before starting the deposition, we evacuated the system to a base pressure of approximately 10^{-4} Pa, thermally purged the chamber and all components therein at the chosen deposition temperature of 500 °C for 30 min and subsequently ion-etched the substrates for 10 min in a pure Ar atmosphere with a pressure of 6 Pa by applying a constant voltage of –750 V to the substrates. The coatings were deposited by applying currents of 600 mA and 1000 mA to the W and Ti targets respectively while bleeding an Ar/N₂ gas mixture with a flow ratio of 5.3 sccm/4.7 sccm into the chamber (while keeping the total pressure at 0.4 Pa). A separate generator was used to apply a constant bias voltage of –40 V to the substrates during the deposition process to ensure the formation of a dense microstructure in our films. The parameters above resulted in deposition rates of 14.7 and 10.6 nm/min for monolithic TiN and WN respectively. The deposition rates of the TiN/WN SLs were reasonably constant around 12.1 nm/min. In all cases, we aimed for total film thicknesses between 1.5 and 3 μm, to ensure reliability of the mechanical testing methods. The approximate sputter yields of the targets under these conditions were 0.34 (2" W) and 0.33 (3" Ti).

Structural investigation of the produced coatings was conducted using a symmetric Bragg-Brentano X-ray diffraction (XRD) setup featuring Cu K α radiation. A Ge (220) hybrid monochromator guaranteed Cu-K α 1 radiation only. The thickness and morphology of the coatings were analysed by taking cross-sectional images of the samples with an FEI Quanta 250 FEG (a field emission gun scanning electron microscope – FEGSEM).

The microstructure of the TiN/WN films was investigated by a JEOL 2100F field emission microscope (200 kV) equipped with an image-side C_s-corrector. The cross-sectional TEM samples were prepared using a standard sample preparation approach including grinding, polishing, dimpling, and ion-milling. The exposure time for the HRTEM images was set to 1.0 s. The aberration coefficients were set to be sufficiently small, under which the HRTEM images were taken under slightly over-focus conditions (close to Scherzer defocus). STEM images shown in this paper were recorded using a high-angle annular dark-field (HAADF) detector, with the detector inner angle/outer angle set to 54 mrad/144 mrad, respectively. Under these conditions, the STEM-HAADF contrasts are nearly proportional to the atomic number (Z-contrast image).

The fracture toughness of all thin films was unveiled by performing pre-notched single cantilever bending experiments of freestanding coating material [35]. These cantilevers were prepared with a focussed ion beam (FIB) workstation (FEI Quanta 200 3D DFIB), which was also used to remove the substrate material beneath the cantilevers. These cavities below the coating were cut using subsequent steps of 5 nA, 3 nA and 500 pA, lowering the ion beam current for cuts close to the film material. The cantilevers themselves were cut with 1 nA to obtain the rough shape and 500 pA for fine patterning steps. A pre-crack was incised into each cantilever with an ion beam current of 50 pA. We chose an acceleration voltage of 30 kV for all FIB processes and aimed for dimensions of roughly $t \times t \times 7t$ for all cantilevers, where t refers to the coating thickness (in μm). The bending tests were executed

inside the aforementioned FEGSEM by a PI85 PicoIndenter (Hysitron). The spherical diamond tip attached to the indenter had a tip radius of about 1 μm. Selecting a rate of 5 nm/s for the displacement controlled bending processes, we loaded the cantilevers until failure. The maximum recorded force F_f at failure as well as the actual dimensions of the cantilevers – determined by measuring the fracture cross-section and the lever arm in the SEM – were all used to derive a value for the critical stress intensity K_{IC} (in MPa√m) for each of our coatings. These calculations relied on the model established by Matoy et al. [36], which is based on linear elastic fracture mechanics and is mainly constituted by the following two formulae:

$$K_{IC} = \frac{F_f l}{b w^{3/2}} f\left(\frac{a_0}{w}\right) \quad (2)$$

Wherein $f(a_0/w)$ denotes a polynomial shape function with the following definition:

$$f\left(\frac{a_0}{w}\right) = 1.46 + 24.36\left(\frac{a_0}{w}\right) - 47.21\left(\frac{a_0}{w}\right)^2 + 75.18\left(\frac{a_0}{w}\right)^3 \quad (3)$$

In the equations above, l stands for the length of the cantilever, b for the breadth and w for thickness of the freestanding coating material. The depth of the pre-existing crack a_0 usually fell within the range of 0.15 t to 0.28 t .

To shed light onto the hardness values and Young's moduli of the thin films we worked with a Fischer Cripps Laboratories ultramicroindentation system (UMIS) fitted with a Berkovich indenter tip. In total, 31 indents were inflicted upon each specimen with forces ranging from 3 mN to 45 mN. To keep the influence of the substrate on the measurements at a minimum, all indents that exceeded a depth of 10% of the coating thickness were disregarded. The indentation modulus of each coating was deduced by combining the reduced modulus provided by the nanoindenter with the DFT-calculated Poisson's ratio in accordance with the method outlined by Fischer-Cripps [37].

Lastly, whenever possible, measurements in this document are quoted and shown in terms of their sample mean and standard error. This is to estimate the accuracy of the calculated means for a given sample size. For all quantities that we derived from two or more measured properties (e.g. the critical strain energy release rate G_c), we used the rules of error propagation to estimate the standard error of the derived quantity.

3. Results & discussion

3.1. Theoretical studies – structures and mechanical properties

Considering the wide range of stoichiometries exhibited by WN as well as the complex effects of the interface, the structure of TiN/WN superlattices could be rather intricate and may inherently contain a high amount of vacancies. For this reason, we first employ quantum-mechanical simulations to compare several TiN/WN systems ($\Delta \sim 2$ nm) with different vacancy types (Ti, N, W), contents (25, and 50 at.% in a respective sublattice) and spatial distributions (ordered vs. disordered vacancies within all layers vs. vacancies clustered in the interface region) in terms of their chemical stability. In consideration of the MgO (100) substrates that were used for all mechanical testing methods of our project, all the simulation superlattices were designed to have (001) oriented interfaces. Structural analysis of the fully relaxed TiN/WN SL – with no vacancies yet considered – reveals a shift of W and N (001) planes caused by the biaxial coherency stresses. In light of comparable results obtained for metastable MoN/TaN SLs [38], this lowering of

symmetry can be understood by a (partial) elimination of phonon instabilities of the cubic WN through relaxation towards the tetragonal ζ -WN (P4/nmm). The calculated formation energies suggest that WN layers of the SL are substantially stabilised (as compared to the vacancy-free system) when some of the metal and/or non-metal lattice sites remain unoccupied (Fig. 1a).

Contrarily, vacancies distributed within TiN layers are found energetically unfavourable. In line with previous studies [8], WN layers of the most stable TiN/WN superlattice exhibit the NbO-type structure, yielding 25% of both metal and non-metal lattice sites unoccupied. Energetically close are the TiN/W_{0.5}N and TiN/WN_{0.5} modifications. The almost negligible energy differences ~ 0.005 eV/at. (not shown here) between various defect distributions (at a fixed vacancy content and for the same vacancy type) indicate there is no strong preferential site for vacancies. In terms of vibrational stability, the important stabilisation role of vacancies in the WN layers

is clearly underpinned by the calculated phonon density of states (DOS) (Fig. 1b) uncovering non-zero DOS values in the imaginary frequency range (shown as real negative values) of the defect-free SL.

Since imaginary frequencies correspond to soft phonon modes, such a system lacks dynamical stability. A SL architecture containing 50% of the stable TiN is thus still incapable of eliminating phonon instabilities of defect-free WN. Interestingly, also the TiN/W_{0.5}N SL is found vibrationally unstable. Therefore, the structural candidates that can be potentially synthesised in the experiment are the TiN/WN^{NbO} and TiN/WN_{0.5} SLs, exhibiting no imaginary phonon DOS. As formation energies of the two polymorphs are comparable, the stability order depends strongly on the actual choice of the N and metal chemical potentials (Equation (3)). Consequently, the N₂ partial pressure in the reactive sputtering process is expected to present a crucial factor for tuning the chemistry of the TiN/WN SLs.

Though the applied deposition conditions could render various defected SL structures obtainable, some of them might be particularly desirable in terms of mechanical properties. Table 1 reviews elastic response of selected SL configurations (based on Fig. 1) in terms of their polycrystalline bulk, B, shear, G, and Young's moduli, E, together with the monolithic phases for comparison. Mechanical stability of the defect-free SL is achieved for a bilayer period of ~ 3.6 nm (in contrast to ~ 1.9 nm), yet the above phonon calculations (Fig. 1) reveal that this system is vibrationally unstable. Comparably thin nanolaminates (~ 3.3 – 3.5 nm) containing N vacancies are mechanically stable only if their concentration is 50 at. %. Unlike that, both TiN/W_{0.75}N and TiN/W_{0.5}N ensure mechanical stability. In terms of the bulk moduli, the TiN/WN^{NbO} and TiN/WN_{0.5} modifications score comparably high (~ 300 GPa), exceeding SLs with 50 at. % of W vacancies above ~ 80 GPa. The overall polycrystalline Young's modulus maximum of 452 and 478 GPa is predicted for the TiN/WN^{NbO} superlattice with bilayer period ~ 1.69 and ~ 3.4 nm, respectively.

In order to preselect structural candidates with exceptional toughness, we correlate the DFT calculated bulk-to-shear modulus ratio, B/G, with the Cauchy pressure of various conventional nitride (SL) coatings, as well as those of TiN/WN SLs and their constituents (Fig. 2). The semi-empirical Pugh and Pettifor criteria [39,40] (in combination with the results in Table 1) point towards a highly disparate character of WN depending on its exact structural configuration. The TiN/WN_x SLs noticeably outclass established binary TMNs and nitride SLs. The other stable cubic polymorph of WN, the NbO-type structure, in contrast, scores lowly – both in its monolithic form and in a SL arrangement with TiN – and fails to promise a degree of ductility unachievable by simpler binary TMNs.

The B/G value also links to the Poisson's ratio and hence, can serve as an estimate of the bonding nature of the material [41]. At this stage, it is important to note that the above-mentioned estimates were originally developed for metals. In particular, Poisson's ratio (and in extension also the B/G ratio) was shown to be unreliable when applied to more brittle materials, such as metallic glasses [42]. From that perspective, our results should be treated as qualitative guidelines for ductility rather than as direct and quantitative connections.

Encouraged by the predicted stability, promising elastic properties as well as outstanding theoretical ductility of TiN/WN_{0.5}, we commenced the synthesis of the desired SLs and constituents, wary of the careful manipulation of the processing conditions necessary to enable the formation of these structures.

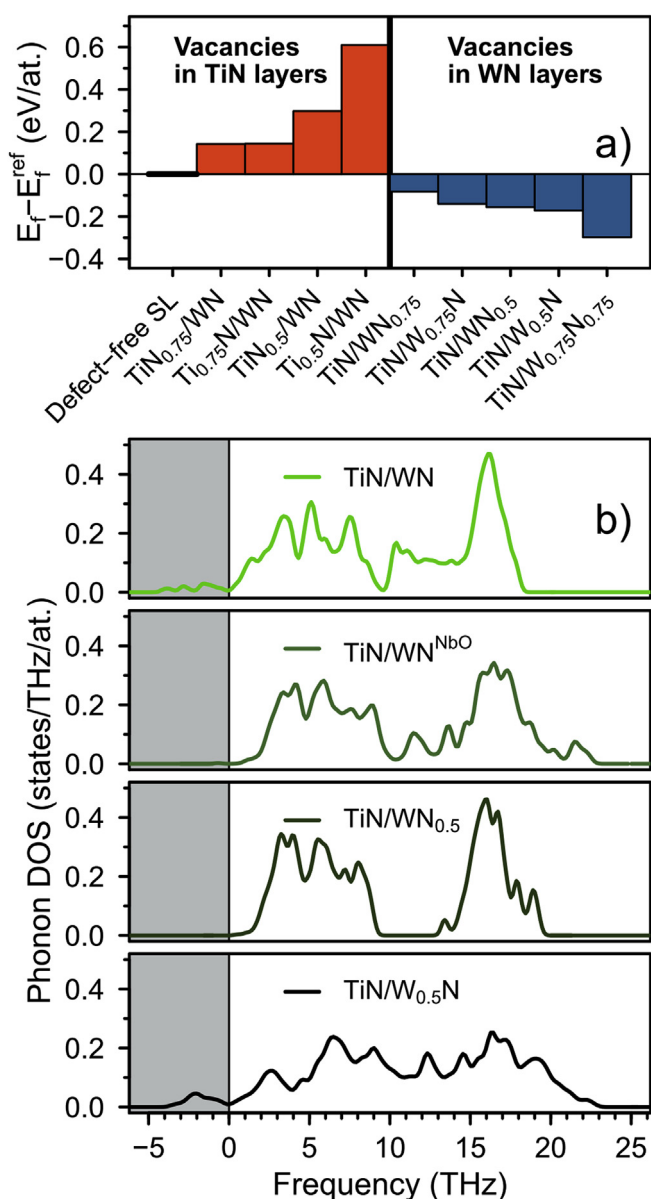


Fig. 1. Visualisation of (a) the difference between the formation energy of the defect-free and the vacancy-containing superlattice, considering various species and concentrations of absent atoms. (b) Phonon density of states (DOS) corresponding to the defect-free superlattice compared to the lowest-energy defected variants.

3.2. XRD analyses

The X-ray diffraction (XRD) patterns show face-centered cubic

used them for all further depositions. The peaks of monolithic WN deposited in such a reactive atmosphere coincide most closely with our referential DFT-calculated pattern of rs-WN_{0.625} (with the same formation energy ~ -0.71 eV/at. as rs-WN_{0.5}). Such a departure in stoichiometry from rs-WN_{0.5} is a relatively common observation, as past studies have reportedly reached N vacancy concentrations of as low as 7% in the rocksalt structure [11]. However, residual stresses can also influence the peak positions [44]; estimations of the vacancy concentration solely based on peak shifts are thus rather limited in accuracy. Moreover, it should be noted that minor differences between experimental and theoretical XRD patterns may be a result of the well-known overestimation of the lattice constants by the GGA-DFT method.

The XRD patterns of all coatings grown on MgO (100) platelets (Fig. 4b), which were used for all further analyses, depict a clear (100) texture. The derivable lattice parameters of TiN and WN on MgO (100) are essentially identical to those on Si (100), since the (200) peaks on both substrates occur at virtually the same diffraction angle (please note that, in this approximation, we neglect the effect of macro-stresses on the peak position). Multilayers on both substrates – Si (100) and MgO (100) (Fig. 4a and b, respectively) – show distinct satellite peaks, which suggests the presence of a superlattice structure with sharp interfaces in most TiN/WN coatings. The nanolaminates with the highest and lowest bilayer period pose the only exceptions to this trend as they fail to show satellite peaks of significant intensity. For the coating with the highest bilayer period, this behaviour is expected, since its bilayer period was estimated by SEM measurements to be 167 nm. At such high Δ -values, the satellite peaks would effectively merge with the main Bragg peaks, see for instance Ref. [45]. For the SL with the lowest bilayer period (2.8 nm), this disappearance of the satellite peaks could be indicative of interdiffusion between the layers, partially replacing the sharp interfaces between TiN and WN with a ternary TiWN interphase.

Out of all the reference patterns of the DFT-proposed structures, the synthesised TiN/WN superlattices align most closely with that of the rocksalt-based cubic TiN/WN_{0.5} structure. In fact, the TiN/WN SLs show a better agreement with the simulated structure featuring a nitrogen vacancy concentration of 50% within the WN layers than the monolithic films. This indicates that the SL architecture

facilitates the stabilisation of WN layers with vacancy concentrations unattainable by the bulk materials at the same deposition conditions. Moreover, we calculated a reference XRD pattern for a theoretical TiN/WN^{NbO} SL structure with a bilayer period of 3.64 nm based on the theoretical lattice parameter, which we used to extrapolate an fcc peak sequence. Upon close analysis, we were unable to detect an alignment of our experimental peak positions with the calculated ones in Fig. 4a, suggesting an absence of this phase in our coatings. Also, a full simulated reference pattern of WN^{NbO} (not depicted) reveals additional peaks, as a consequence of vacancy ordering, which are not covered by the standard fcc sequence seen in our experimental data (Figs. 3 and 4). Lastly, the XRD data presented in Figs. 3 and 4 also excludes rs-W_{0.5}N, as well as TiN/W_{0.5}N as possible constituents of our monolithic WN and TiN/WN SLs respectively. These phases were already found to be dynamically unstable by our calculations (see previous section), and the comparison of the experimental XRD-derived lattice parameters of our WN and TiN/WN (~ 4.25 Å) with the calculated lattice parameters of the W-deficient structures (Table 1) further reinforces our notion that these structures are non-existent in our synthesised films.

The coatings on Si (100) were only used for XRD analyses, because Si facilitates the growth of polycrystalline films, which show the full fcc peak sequence, making the comparisons of our experimental XRD patterns with referential patterns considerably clearer. TMN thin films on MgO (100) are usually highly textured and produce a (200) peak only.

3.3. HRTEM analyses

An overview of high-angle annular dark field scanning transmission electron microscopy (HAADF-STEM) images of epitaxial TiN/WN multilayers with bilayer periods Δ of 2.8 nm, 8 nm and 10.2 nm on MgO (100) is presented in Fig. 5a, b and c, in which the distinct contrast represents the WN (bright) and TiN (dark) layers. Accordingly, three typical HRTEM phase contrast images recorded all along the [001] viewing direction are displayed in Fig. 5d ($\Delta = 2.8$ nm), Fig. 5e ($\Delta = 8$ nm), and Fig. 5f ($\Delta = 10.2$ nm), respectively. The atomically resolved HRTEM images clearly reveal the bilayer atomic structure, in which respective TiN and WN layers (labeled) are distinguished, and interface atomic structure.

The Fast Fourier Transform (FFT) patterns of the HRTEM images (insets) confirm the presence of stabilised fcc phase in the multilayers, which is consistent with the XRD measurement, and further indicate a close match of the lattice constants between the layers, supporting our previous conclusions on the structure in the WN layers. According to the atomic resolution images, it is also noticed that there are dislocations (exemplified in Fig. 5f) and more distorted regions (labeled by arrows in Fig. 5f) distributed within the WN layers. The [100] growth direction and cubic/cubic coherent interfaces are also found in Fig. 5d ($\Delta = 2.8$ nm), Fig. 5e ($\Delta = 8$ nm), and Fig. 5f. The measured interplanar spacing of WN layers, $d_{(200)}$, is 0.210 nm in Fig. 5d, 0.210 nm in Fig. 5e and 0.209 nm in Fig. 5f. These values show an excellent agreement with the calculated lattice parameter of rs-WN_{0.5} (4.181 Å, see Table 1).

3.4. Nanoindentation

The hardness data of coatings deposited on MgO (100) presented in Fig. 6a shows that all TiN/WN superlattice structures possess higher readings than the monolithic TiN and WN coatings. A clear maximum of 36.7 ± 0.2 GPa is uncovered for the TiN/WN SL with a bilayer period of 8.1 nm. Above and below that bilayer period, the hardness of the TiN/WN system declines distinctly and can be fitted by logarithmic trends in accordance with the model of

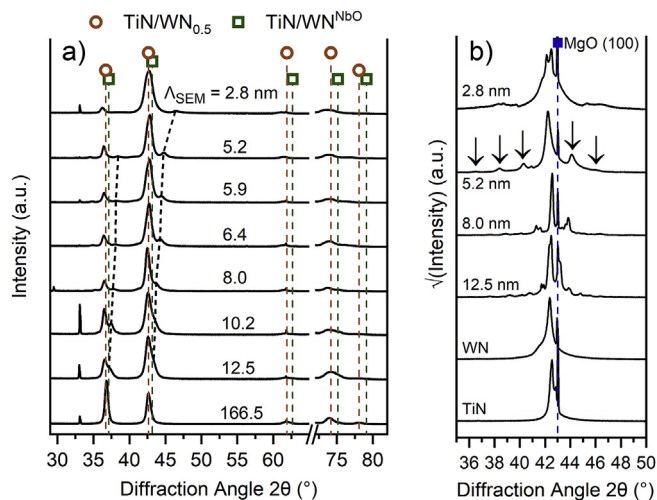


Fig. 4. X-ray diffraction patterns of all SL coatings deposited on Si (100) (a) and of selected coatings deposited on MgO (100) (b). The arrows in (b) exemplify the positions of satellite peaks, the dashed black line in (a) illustrates the progression of these satellite peaks with changing bilayer period. The referential peak positions for the two variant SL structures were calculated by DFT.

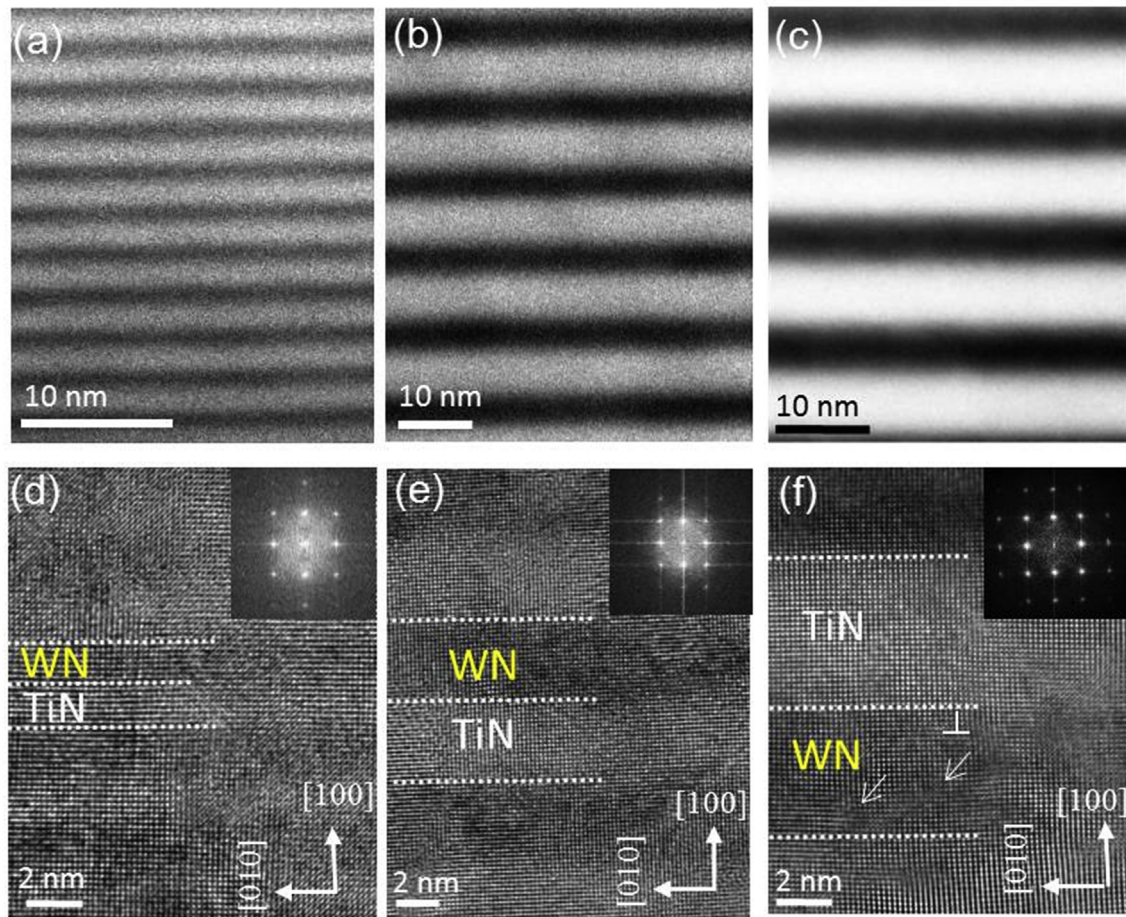


Fig. 5. Cross-sectional HAADF-STEM and HRTEM images of the TiN/WN multilayer coatings with bilayer periods Λ of 2.8 nm (a and d), 8 nm (b and e) and 10.2 nm (c and f). Distorted regions in WN are indicated by arrows.

Chu and Barnett [2]. Due to the very close match of the lattice parameters as obtained from XRD, it seems reasonable that our TiN/WN SLs roughly follow a model that neglects coherency strains and centres on differences in the elastic moduli of the layers.

The hardness values recorded for TiN and WN reside at 31.7 ± 0.2 GPa and 32.0 ± 0.4 GPa, respectively. In contrast, the indentation modulus of films on MgO (100) (Fig. 6b) shows a minimum of 387 ± 2 GPa for a SL structure with a bilayer period of 12.5 nm. Together with the TiN/WN coating featuring a bilayer period of 10.2 nm, this specimen seemingly fails to adhere to the rule of mixture, as its indentation modulus falls below those of both monolithic coatings. In fact, all other SL films exhibit indentation moduli that lie between those of the plain constituents. However, the XRD patterns and HRTEM images implied a difference in vacancy concentration between the monolithic WN and the WN layers in the SLs. Therefore, the monolithic WN is an imprecise reference for the SLs. While in the case of TiN the indentation modulus of 452 ± 3 GPa agrees perfectly with the ab initio polycrystalline Young's modulus $E \sim 451$ GPa (cf. Table 1), the 389 ± 4 GPa recorded for the WN coating resides above the polycrystalline Young's moduli calculated for WN_x structures (Table 1), but still below the $E_{[100]}$ value of $\beta\text{-WN}_{0.5}$ (448 GPa), a variant r-structure featuring ordered vacancies on the N-sublattice. Therefore, this deviation may be caused by small differences in the vacancy concentration and distribution between theory and experiment.

The indentation moduli of the SLs consistently fall in between

the calculated polycrystalline and directional [100] Young's moduli. This set of data thus cannot serve as the sole confirming factor for any structural questions. However, the substantial divergence of the theoretical Young's modulus of WN^{NbO} from our experimental readings further reinforces the previously established notion that this phase is absent from our coatings. The two entities – hardness and indentation modulus – were combined to deduce an H/E ratio, depicted in Fig. 6c, unveiling that the SL structure in general enhances this empirical indicator of toughness. Also, the H/E ratio of TiN/WN SLs is noticeably maximised by a bilayer period of 10.2 nm.

3.5. Fracture toughness evaluation

The results of the micromechanical bending tests of coatings on MgO (100) are presented in Fig. 7a in terms of the calculated critical stress intensity K_{IC} . Perhaps the most striking feature in Fig. 7a is the strongly pronounced dependence of the fracture toughness on the bilayer period. The highest fracture toughness was 4.6 ± 0.2 $\text{MPa}\sqrt{\text{m}}$ for the SL coating with a bilayer period of 10.2 nm. The maximum constitutes an increase of K_{IC} of 67% compared to monolithic TiN and 53% compared to the pure WN coating, for which we measured values of 2.8 ± 0.1 $\text{MPa}\sqrt{\text{m}}$ and 3.1 ± 0.1 $\text{MPa}\sqrt{\text{m}}$, respectively. To put that into perspective, other coatings grown within the same deposition system and tested via the same procedure as the TiN/WN films were TiN/CrN SLs, TiSiN (both grown on Si (100)) and TiAlN (grown on Al_2O_3 (1 $\bar{1}$ 02) platelets). Depending on their bilayer period or composition, these

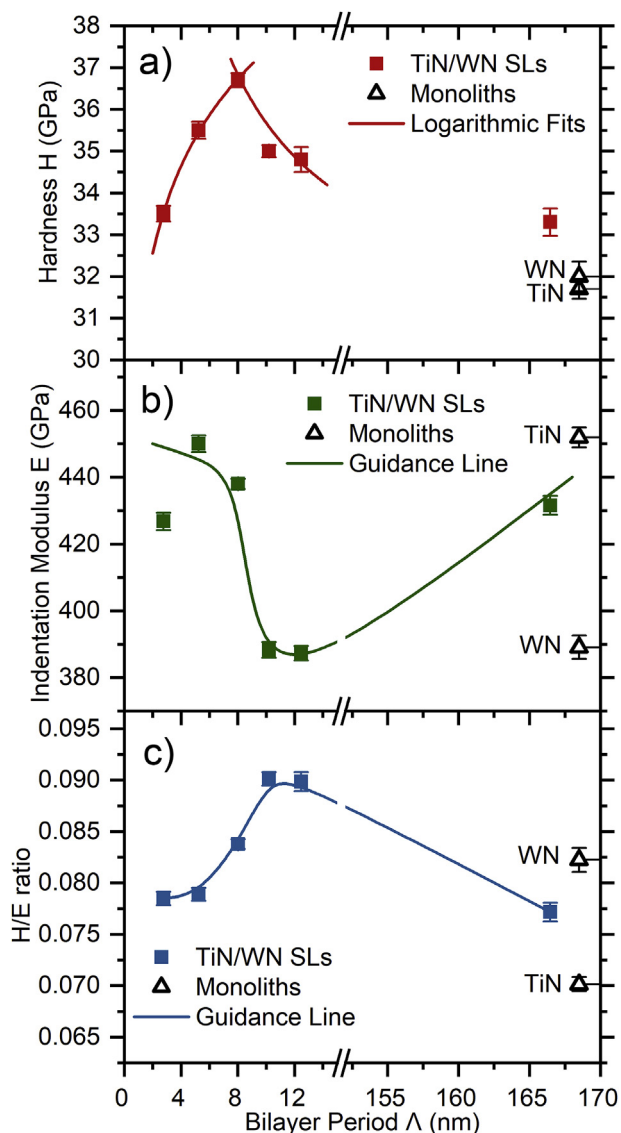


Fig. 6. Plots of hardness (a), indentation modulus (b), and the H/E ratio of the monolithic coatings and of the SLs as a function of the bilayer period.

materials reached maxima of 2.0, 3.0 and 2.7 (as deposited) $\text{MPa}\sqrt{\text{m}}$ respectively [4,46,47]. TiAlN and TiAlTaN deposited in an industrially scaled arc evaporation system exhibited maximum fracture toughness readings of 3.5 and 4.7 $\text{MPa}\sqrt{\text{m}}$, respectively [48].

Moving below and beyond a bilayer period of 10.2 nm, the values decrease markedly, but consistently surpass the monolithic coatings – a trend that mimics the behaviour of the H/E ratio presented further above. This suggests an interplay between at least two different mechanisms. The right-hand sided branch of the trend – showing an increase of the fracture toughness and decrease of Young's modulus – with decreasing bilayer period may be caused partially by changes of the bonding characteristics in the material. Furthermore, a proportionality of $1/\sqrt{\Delta}$ can be fitted to the three points along this branch of the trend. In doing so, our fracture toughness trend shows similarities to the predicted fracture strength enhancement of laminar composites consisting of layers with vastly different elastic moduli [49].

Since the HRTEM and HAADF images in Fig. 5d–f, as well as the XRD patterns, indicate that the $rs\text{-WN}_{0.5}$ structure is stabilised in

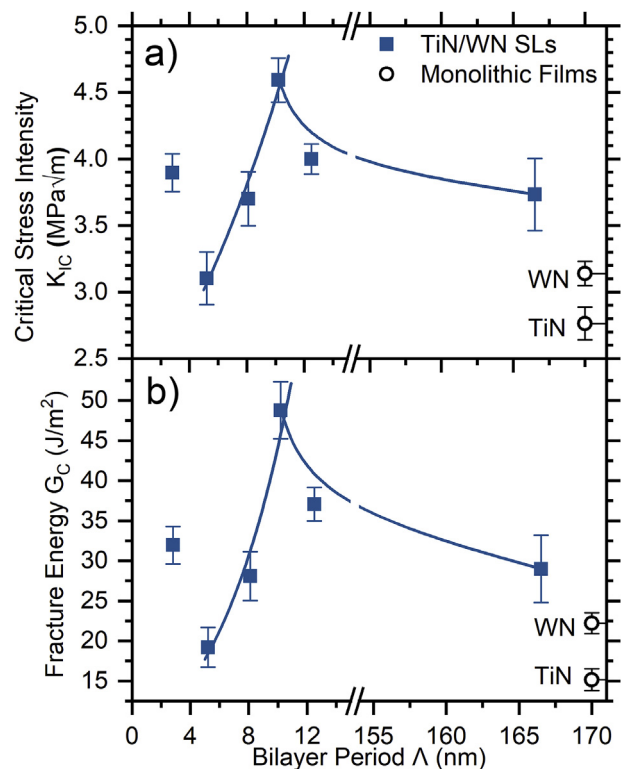


Fig. 7. Plot of the critical stress intensity (a) and the critical strain energy release rate (b) against the bilayer period for TiN/WN superlattices. The values of the monolithic coatings are included as references.

the WN layers of the SLs with bilayer periods at and above the fracture toughness peak, the elastic moduli of the WN in these films differ significantly from those of TiN (theoretical values given in Table 1). Thus, we assume that these significant periodic fluctuations of the elastic properties across the film are the main contributing factor of the fracture toughness enhancement with decreasing bilayer period. We envision that the decreasing fracture toughness with decreasing bilayer period could be attributed to a gradient of the nitrogen concentration in the WN layers close to the interface. WN in the bulk of the layers appears to lie rather close to $rs\text{-WN}_{0.5}$ in stoichiometry, according to our XRD patterns and HRTEM images. However, a more detailed comparison of the (200) peak positions of the SL with bilayer periods of 8 nm and 5.2 nm uncovers a miniscule downward shift of the diffraction angle. This could be associated with an enlargement of the lattice parameter, due to a higher occupancy of the nitrogen sites.

The high-energy-environment during sputtering, as a result of the elevated deposition temperature combined with the impact energy of the sputtered atoms, could induce diffusion of nitrogen between the perfect stoichiometric TiN and the vacancy-rich WN. Due to the dependence of the mechanical properties of WN on the defect type and concentration (see Fig. 2 and Table 1), a varying degree of N-vacancies along the interfaces could noticeably alter the fracture properties of TiN/WN SLs with a lower bilayer period and thus higher concentration of interfaces. A larger proportion of a stiffer phase within the WN layers would also diminish the markedness of elastic fluctuations, leading to a decrease of both the fracture toughness and the elastic fracture energy.

Lastly, the SL with the lowest bilayer period evidently diverges from the suggested trend, showing an increase of K_{IC} compared to the next lowest bilayer period. In combination with the diminished intensity of the satellite peaks recorded for that coating, the trend-

breaking value serves as a strong testimony to the formation of a ternary TiWN across the interfaces. The literature generally ascribes a high potential for toughness to this compound, which would coincide with our measurements [12,50]. Fig. 7 may evoke the impression that the outlier deviates from the rule of mixture, however, the reference for the properties of TiWN would be a theoretical pure rs -WN_{0.5}, which we did not observe in our monolithic WN coating.

We further combined our experimental results from the bending tests and nanoindentation with our DFT-calculated Poisson's ratios to derive an estimate of the fracture energy (i.e. the critical strain energy release rate) G_C (in J/m²) via the basic relationship for plane strain conditions in Equation (4) [51]. Therein ν represents the Poisson's ratio and E the Young's modulus in Pa.

$$G_C = K_{IC}^2 \left(\frac{1 - \nu^2}{E} \right) \quad (4)$$

This methodology is accompanied by inherent limitations. Firstly, the indentation modulus derived from nanoindentation measurements may deviate from the actual Young's modulus. Secondly, the bilayer periods of the majority of our SL coatings reside above the explorable realm of DFT calculations. Thus, we assumed the Poisson's ratio of 0.32 calculated for TiN/WN_{0.5} with $\Delta = 3.327$ nm to remain constant for higher bilayer periods, since the Poisson's ratios in Table 1 appear to stabilise around this value. Also, this theoretical bilayer period already overlapped with our experimental ones. Lastly, plane strain is an idealised scenario, which represents the geometry of our cantilevers fairly closely. For the contrasting case (i.e. plane stress), the $(1 - \nu^2)$ -term disappears, increasing all our readings by roughly 10%. Following this model, we derive fracture energies of 15.2 ± 1.4 and 22.2 ± 1.3 J/m² for our monolithic TiN and WN films, respectively. The TiN/WN SL with a bilayer period of 10.2 nm reaches an impressive fracture energy of 48.8 ± 3.5 J/m², which is roughly triple the value measured for TiN.

The cross-sectional SEM micrographs of the fracture surface reflect the conclusions drawn from the micromechanical bending tests. Firstly, Fig. 8a shows an illustrative SEM image of the spherical indenter tip and a cantilever directly before testing. Fig. 8b

through 8f depict various cross sections of cantilevers after testing. The fracture surface of a cantilever belonging to the sample with highest bilayer period (Fig. 8b) shows a small degree of delamination, predominantly in the WN layers, suggesting that deformation is concentrated in the more compliant WN layers. In contrast to Fig. 8b, the fracture surfaces of TiN (Fig. 8c) and WN (Fig. 8d) have a much smoother appearance, implying that crack propagation is more energetically demanding in the nano-laminated structures.

Furthermore, Fig. 8c depicts a distinctly brittle and intergranular fracture surface for TiN. WN and two more exemplary TiN/WN SLs feature a less faceted texture (Fig. 8d–f). The TiN/WN specimens (Fig. 8e and f) in particular show a series of fine fracture lines that originate at the narrow bridges. The pattern of the fracture lines concurs with simulations of Brinckmann et al., who predicted the bridges to be the region where a crack would nucleate [35]. Also, their model recommends displacement controlled tests on cantilevers with narrow bridges and deep notches in order to obtain the most accurate critical stress intensity values [32]. While we conducted all our tests displacement-controlled, it is apparent that the geometries of the WN and TiN/WN samples depicted in Fig. 8 adhere more closely to these criteria than the TiN cantilevers.

The higher degree of deformability implied by both the toughness data in Fig. 7, as well as the micrographs in Fig. 8 is confirmed by the load-deflection curves. Based on cross-sectional SEM images we measured a thickness of 2.6 μ m for TiN and around 1.9 μ m for WN, as well as the represented TiN/WN SLs. The resulting size differences of the cantilevers are unaccounted for in the absolute deflection plotted against the applied force in Fig. 9a. In Fig. 9b, however, the dimensions are considered, as the stress intensity of one representative cantilever per selected sample is confronted with the corresponding relative deflection (expressed in %). For this purpose, the absolute deflection values of each presented curve were divided by the thickness of the respective cantilever, as all other dimensions of the cantilevers were chosen in relation to their thickness. The absolute values of this relative deflection on their own possess limited significance; however, they enable a qualitative comparison between the coatings. The normalised curves

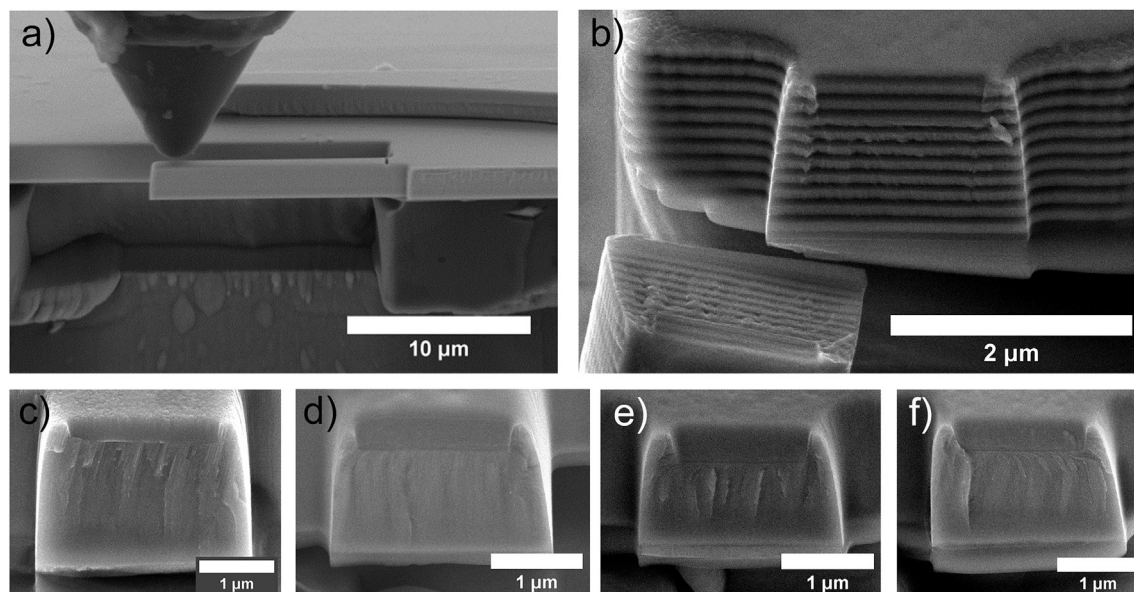


Fig. 8. SEM micrographs of a cantilever, cavity and the indenter before testing (a), as well as several fracture cross sections. (b) shows an enhanced cross-section of the TiN/WN SL with a bilayer period of 166.7 nm. (c) and (d) represent TiN and WN respectively. The fracture surfaces of the toughest ($\Delta = 10.2$ nm) and least tough ($\Delta = 5.2$ nm) SLs are depicted accordingly in (e) and (f).

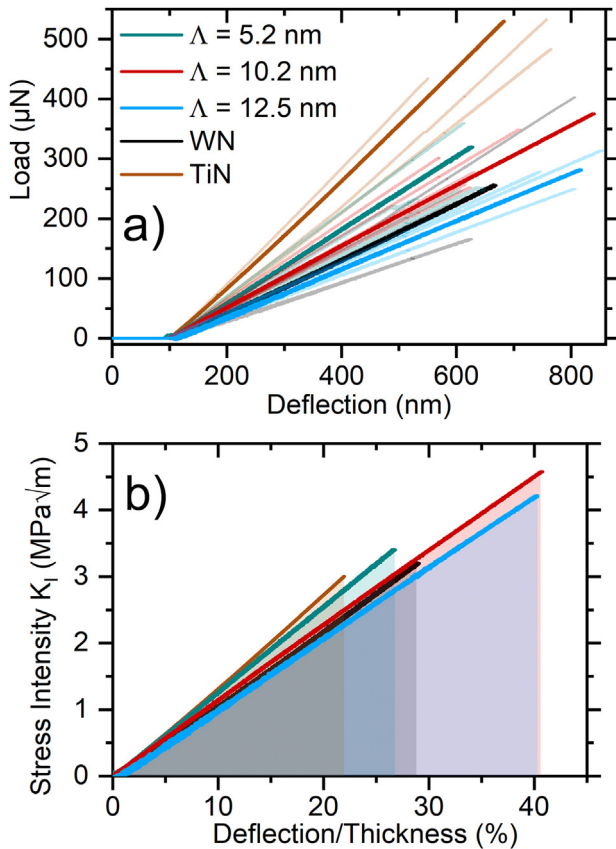


Fig. 9. Load-deflection curves (a) and plots of the stress intensity vs. the relative deflection in terms of the respective thickness for all cantilevers of TiN, WN, and selected SL coatings. The curves of particularly representative cantilevers are depicted opaquely in (a) and shown in (b).

suggest a two times larger elastic deformability for the toughest TiN/WN superlattices compared to monolithic TiN. In combination with the increased critical stress intensity, this doubled elastic deformation limit contributes towards the substantially enhanced fracture energy (emulated by the shaded areas under the curves). Additionally, the slopes of the curves reflect the trend observed in the indentation modulus, as the coatings with higher indentation moduli also produce a steeper slope in Fig. 9b.

3.6. Modelling-based interpretations of bilayer-dependent trends

In view of the compositional fluctuations (i.e. variations of the vacancy concentration on the N-sublattice) suggested by both XRD and mechanical investigations, we employed the generalised linear elasticity Grimsditch-Nizzoli method (see the Methodology section for details) and simulated bilayer dependent elastic data for various nanolayered systems. Thereby, we aimed to match the observed experimental trend of the indentation modulus, to assess the possible influence of changes in the vacancy concentration and/or the stabilisation of metastable phases in the WN layers of our SL films. The interface region was approximated by either TiN/WN_{0.5} or TiN/WN SLs, while the bulk-like layers in TiN were modelled by rs-TiN. The N vacancy gradient was achieved by changing the volumetric ratio of (i) the tetragonally distorted ζ -WN and (ii) the N substoichiometric rs-WN_x ($x = 0.5-0.88$) within the WN layers. Fig. 10 depicts the Grimsditch-Nizzoli based models succeeding to reproduce the evolution of indentation data (Fig. 6b) to the highest degree of precision. Notably, depending on the chosen

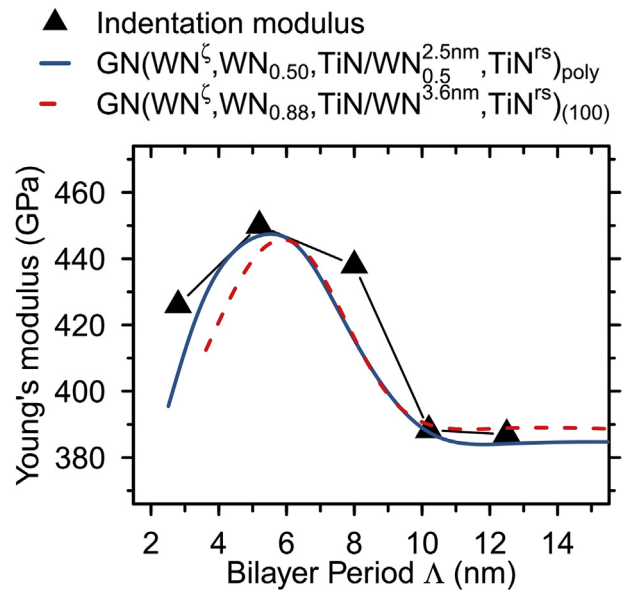


Fig. 10. Comparison of experimental indentation moduli with theoretically calculated bilayer-dependent Young's moduli (based on the Grimsditch-Nizzoli method).

approximation of the interface - TiN/WN_{0.5} or TiN/WN SLs - either the polycrystalline Young's modulus or the (100) directional variant resulted in a reasonable agreement with the experiment.

The model implementing interface effects through the 2.5 nm TiN/WN_{0.5} SL leads to a hypothesis that the indentation moduli below and at the peak at $\Lambda \approx 6$ nm originates from populating the N sublattice in the WN layers. Specifically, the volume fraction of the stoichiometric ζ -WN in WN layers increases (to the detriment of rs-WN_{0.5}) from ~20 to 40 at. %. The indentation modulus decrease at higher Λ can be attributed (i) to the diminishing contribution of interfaces and (ii) to the fact that a partial stabilisation (20–40 at. % in the WN layers) of (nearly) stoichiometric WN in the SL is no longer possible (similarly to, e.g., cubic AlN which can form in AlN/TiN, AlN/TiAlN and AlN/CrN SLs only if its thickness does not exceed ~2 nm [52–56]). The second model based on the defect-free 3.6 nm TiN/WN interface suggests that the ζ -WN constitutes ~85 at. % of the WN layers below and at the peak at $\Lambda \approx 6$ nm. The volume fraction of the stoichiometric WN, however, decreases rapidly when going to higher bilayer periods and the rs-WN_{0.88} (expectably also the rs-WN_{0.50}) is stabilised instead.

All in all, the above findings clearly speak for fluctuations of the vacancy concentration across the WN layers in our SL thin films. The proposed compositional evolution may further shed light on the trends in fracture toughness. As a next step, we calculated cleavage energy, E_c , for brittle cleavage and estimated K_{IC} according to a simple formula

$$K_{IC} = \sqrt{cE_{hkl}E_c} \quad (5)$$

where E_{hkl} represents directional Young's modulus and c is a scaling factor, conventionally set to 4 [57]. To properly represent the experimental data, SLs were cleaved perpendicular to the interfaces. Supporting the experimental finding that our SL coatings outperform their monolithic constituents, the 2.5 nm TiN/WN_{0.5} interface ($K_{IC} \sim 2.92$ MPa√m) exceeds the fracture toughness of the monolithic WN_{0.5} ($K_{IC} \sim 2.66$ MPa√m) and TiN ($K_{IC} \sim 2.50$ MPa√m). These results, however, are incapable of reproducing the complete experimental bilayer-dependent K_{IC} trend.

Essentially, the overall K_{IC} of the SL may reflect the fracture

behaviour of the individual layer components (featuring, moreover, inhomogeneous defect distributions) in a very intricate fashion. The strong WN and the interface layers can be substantially weakened in a SL arrangement, which is not captured by the present simulations. Nevertheless, the model demonstrates that a certain contribution to the overall toughness enhancement can be found on the bonding level.

4. Summary & conclusions

By conducting DFT calculations, we identified TiN/WN_{0.5} superlattices as a feasible system with a supposed potential for ductility clearly exceeding that of the monolithic constituents as well as many other established TMNs. Based on the insight acquired from our calculations we synthesised a series of TiN/WN SLs with varying bilayer periods in addition to monolithic TiN and WN. The desirable composition of WN_{0.5} is achievable only in the SL arrangement, while in the monolithic case a higher occupancy of the N-sublattice was reached under the applied deposition conditions. Lowering the overall amount of nitrogen leads to the formation of metallic W. The experimentally measured maximum fracture toughness of $4.6 \pm 0.2 \text{ MPa}\sqrt{\text{m}}$ for TiN/WN with a bilayer period of 10.2 nm ranks among the highest recorded values within the field of TMNs and significantly surpasses our monolithic TiN and WN – which yielded 2.8 ± 0.1 and $3.1 \pm 0.1 \text{ MPa}\sqrt{\text{m}}$, respectively. This progression of the fracture toughness mirrors the trend of our calculated Pugh's and Pettifor's criteria for these materials, thus confirming their applicability for qualitatively comparing materials of similar categories. Furthermore, the fracture energy of $48.8 \pm 3.5 \text{ J/m}^2$ of our toughest SL coating constitutes an enhancement by a factor of 3 compared to monolithic TiN ($15.2 \pm 1.4 \text{ J/m}^2$). These results underline the effectiveness of the superlattice architecture for improving TMN thin films. We attribute this conspicuous effect to the difference in the elastic constants between TiN and rs-WN_{0.5}. By employing a theoretical model based on the Grimsditch-Nizzoli method, we conclude that the decrease in toughness observed for low bilayer periods, may be caused by the formation of a N-enriched stiff WN-phase along the interfaces. Beyond the toughness evaluation, highlights of our study include a hardness peak of $36.7 \pm 0.2 \text{ GPa}$, a minimum of the indentation modulus of $387 \pm 2 \text{ GPa}$ and a concentration of deformation in the more compliant WN layers within the SL structure.

Acknowledgment

JB, DH, and MB highly acknowledge the financial support of the Austrian Science Fund (FWF): P30341-N36. Additionally, NK greatly appreciates the support from the Austrian Academy of Sciences (DOC scholarship). The computational results presented have been achieved using the Vienna Scientific Cluster (VSC). The authors acknowledge the use of the facilities of USTEM and XRC at TU Wien. We thank the Institute for Mechanics of Materials and Structures (TU Wien) for providing the PicoIndenter PI-85.

References

- [1] U. Helmerson, S. Todorova, S.A. Barnett, J.-E. Sundgren, L.C. Markert, J.E. Greene, Growth of single-crystal TiN/VN strained-layer superlattices with extremely high mechanical hardness, *J. Appl. Phys.* 62 (1987) 481–484, <https://doi.org/10.1063/1.339770>.
- [2] X. Chu, S.A. Barnett, Model of superlattice yield stress and hardness enhancements, *J. Appl. Phys.* 77 (1995) 4403–4411, <https://doi.org/10.1063/1.359467>.
- [3] P.B. Mirkarimi, L. Hultman, S.A. Barnett, Enhanced hardness in lattice-matched single-crystal TiN/V_{0.6}Nb_{0.4}N superlattices, *Appl. Phys. Lett.* 57 (1990) 2654–2656, <https://doi.org/10.1063/1.104189>.
- [4] R. Hahn, M. Bartosik, R. Soler, C. Kirchlechner, G. Dehm, P.H. Mayrhofer,

- Superlattice effect for enhanced fracture toughness of hard coatings, *Scripta Mater.* 124 (2016) 67–70, <https://doi.org/10.1016/j.scriptamat.2016.06.030>.
- [5] H. Wang, H. Zeng, Q. Li, J. Shen, Superlattice supertoughness of TiN/MN (M = V, Nb, Ta, Mo, and W): first-principles study, *Thin Solid Films* 607 (2016) 59–66, <https://doi.org/10.1016/j.tsf.2016.03.061>.
- [6] L. Song, Y.X. Wang, First-principles study of W, WN, WN₂, and WN₃, *Phys. Status Solidi Basic Res.* 247 (2010) 54–58, <https://doi.org/10.1002/psb.200945310>.
- [7] Z. Zhao, K. Bao, D. Duan, F. Tian, Y. Huang, H. Yu, Y. Liu, B. Liu, T. Cui, The low coordination number of nitrogen in hard tungsten nitrides: a first-principles study, *Phys. Chem. Chem. Phys.* 17 (2015) 13397–13402, <https://doi.org/10.1039/C5CP00147A>.
- [8] K. Balasubramanian, S. Khare, D. Gall, Vacancy-induced mechanical stabilization of cubic tungsten nitride, *Phys. Rev. B* 94 (2016) 174111, <https://doi.org/10.1103/PhysRevB.94.174111>.
- [9] B.D. Ozsdolay, C.P. Mulligan, K. Balasubramanian, L. Huang, S.V. Khare, D. Gall, Cubic β -WN_x layers: growth and properties vs N-to-W ratio, *Surf. Coating Technol.* 304 (2016) 98–107, <https://doi.org/10.1016/j.surfcoat.2016.06.079>.
- [10] R. Mateus, M.C. Sequeira, C. Porosnicu, C.P. Lungu, A. Hakola, E. Alves, Thermal and chemical stability of the β -W₂N nitride phase, *Nucl. Mater. Energy.* 12 (2017) 462–467, <https://doi.org/10.1016/j.nme.2017.03.040>.
- [11] B.D. Ozsdolay, C.P. Mulligan, M. Guerette, L. Huang, D. Gall, Epitaxial growth and properties of cubic WN on MgO(001), MgO(111), and Al₂O₃(0001), *Thin Solid Films* 590 (2015) 276–283, <https://doi.org/10.1016/j.tsf.2015.08.002>.
- [12] F. Pachter, P.H. Mayrhofer, D. Holec, Vacancy-driven extended stability of cubic metastable Ta–Al–N and Nb–Al–N phases, *Surf. Coating Technol.* 326 (2017) 37–44, <https://doi.org/10.1016/j.surfcoat.2017.07.012>.
- [13] F.F. Klimashin, H. Euchner, P.H. Mayrhofer, Computational and experimental studies on structure and mechanical properties of Mo–Al–N, *Acta Mater.* 107 (2016) 273–278, <https://doi.org/10.1016/j.actamat.2016.01.063>.
- [14] F.F. Klimashin, H. Riedl, D. Primetzhofer, J. Paulitsch, P.H. Mayrhofer, Composition driven phase evolution and mechanical properties of Mo–Cr–N hard coatings, *J. Appl. Phys.* 118 (2015) 25305, <https://doi.org/10.1063/1.4926734>.
- [15] D.G. Sangiovanni, V. Chirita, L. Hultman, Electronic mechanism for toughness enhancement in Ti_xM_{1-x}N (M=Mo and W), *Phys. Rev. B - Condens. Matter Mater. Phys.* 81 (2010) 104107, <https://doi.org/10.1103/PhysRevB.81.104107>.
- [16] D. Holec, M. Friák, J. Neugebauer, P.H. Mayrhofer, Trends in the elastic response of binary early transition metal nitrides, *Phys. Rev. B* 85 (2012) 064101, <https://doi.org/10.1103/PhysRevB.85.064101>.
- [17] D.V. Suetin, I.R. Shein, A.L. Ivanovskii, Elastic and electronic properties of hexagonal and cubic polymorphs of tungsten monocarbide WC and mononitride WN from first-principles calculations, *Phys. Status Solidi* 245 (2008) 1590–1597, <https://doi.org/10.1002/psb.200844077>.
- [18] G. Kresse, J. Furthmüller, Efficient iterative schemes for ab initio total-energy calculations using a plane-wave basis set, *Phys. Rev. B* 54 (1996) 11169–11186, <https://doi.org/10.1103/PhysRevB.54.11169>.
- [19] G. Kresse, D. Joubert, From ultrasoft pseudopotentials to the projector augmented-wave method, *Phys. Rev. B* 59 (1999) 1758–1775, <https://doi.org/10.1103/PhysRevB.59.1758>.
- [20] W. Kohn, L.J. Sham, Self-consistent equations including exchange and correlation effects, *Phys. Rev.* 140 (1965) A1133–A1138, <https://doi.org/10.1103/PhysRev.140.A1133>.
- [21] J.P. Perdew, K. Burke, M. Ernzerhof, Generalized gradient approximation made simple, *Phys. Rev. Lett.* 77 (1996) 3865–3868, <https://doi.org/10.1103/PhysRevLett.77.3865>.
- [22] S.H. Wei, L.G. Ferreira, J.E. Bernard, A. Zunger, Electronic properties of random alloys: Special quasirandom structures, *Phys. Rev. B* 42 (1990) 9622–9649, <https://doi.org/10.1103/PhysRevB.42.9622>.
- [23] F. Birch, Finite elastic strain of cubic crystals, *Phys. Rev.* 71 (1947) 809–824, <https://doi.org/10.1103/PhysRev.71.809>.
- [24] A. Togo, F. Oba, I. Tanaka, First-principles calculations of the ferroelastic transition between rutile-type and CaCl₂-type SiO₂ at high pressures, *Phys. Rev. B - Condens. Matter Mater. Phys.* 78 (2008) 134106, <https://doi.org/10.1103/PhysRevB.78.134106>.
- [25] Y. Le Page, P. Saxe, Symmetry-general least-squares extraction of elastic coefficients from ab initio total energy calculations, *Phys. Rev. B - Condens. Matter Mater. Phys.* 63 (2001) 174103, <https://doi.org/10.1103/PhysRevB.63.174103>.
- [26] Y. Le Page, P. Saxe, Symmetry-general least-squares extraction of elastic data for strained materials from ab initio calculations of stress, *Phys. Rev. B* 65 (2002) 104104, <https://doi.org/10.1103/PhysRevB.65.104104>.
- [27] R. Yu, J. Zhu, H.Q. Ye, Calculations of single-crystal elastic constants made simple, *Comput. Phys. Commun.* 181 (2010) 671–675, <https://doi.org/10.1016/j.cpc.2009.11.017>.
- [28] M. Moakher, A.N. Norris, The closest elastic tensor of arbitrary symmetry to an elasticity tensor of lower symmetry, *J. Elast.* 85 (2006) 215–263, <https://doi.org/10.1007/s10659-006-9082-0>.
- [29] A. Reuss, Berechnung der Fließgrenze von Mischkristallen auf Grund der Plastizitätsbedingung für Einkristalle, *ZAMM - Zeitschrift Für Angew. Math. Und Mech.* 9 (1929) 49–58, <https://doi.org/10.1002/zamm.1929009104>.
- [30] W. Voigt, *Lehrbuch der kristallographie (mit ausschluß der kristallographie)*, B.G. Teubner [J.W. Edwards], Ann Arbor, Mich., Leipzig; Berlin, 1928.
- [31] J.F. Nye, *Physical Properties of Crystals: Their Representation by Tensors and*

- Matrices, Clarendon Press, 1985. https://books.google.at/books/about/Physical_Properties_of_Crystals.html?id=ugwqj-uVB44C&redir_esc=y. (Accessed 9 January 2019).
- [32] M. Grimsditch, F. Nizzoli, Effective elastic constants of superlattices of any symmetry, *Phys. Rev. B* 33 (1986) 5891–5892, <https://doi.org/10.1103/PhysRevB.33.5891>.
- [33] P. Lazar, J. Redinger, R. Podloucky, Density functional theory applied to V N / Ti N multilayers, *Phys. Rev. B* 76 (2007) 174112, <https://doi.org/10.1103/PhysRevB.76.174112>.
- [34] P. Reháč, M. Černý, D. Holec, Interface-induced electronic structure toughening of nitride superlattices, *Surf. Coating. Technol.* 325 (2017) 410–416, <https://doi.org/10.1016/j.surfcoat.2017.06.065>.
- [35] S. Brinckmann, K. Matoy, C. Kirchlechner, G. Dehm, On the influence of microcantilever pre-crack geometries on the apparent fracture toughness of brittle materials, *Acta Mater.* 136 (2017) 281–287, <https://doi.org/10.1016/j.actamat.2017.07.014>.
- [36] K. Matoy, H. Schönherr, T. Detzel, T. Schöberl, R. Pippan, C. Motz, G. Dehm, A comparative micro-cantilever study of the mechanical behavior of silicon based passivation films, *Thin Solid Films* 518 (2009) 247–256, <https://doi.org/10.1016/j.tsf.2009.07.143>.
- [37] A.C. Fischer-Cripps, Critical review of analysis and interpretation of nano-indentation test data, *Surf. Coating. Technol.* 200 (2006) 4153–4165, <https://doi.org/10.1016/j.surfcoat.2005.03.018>.
- [38] N. Koutná, D. Holec, M. Friák, P.H. Mayrhofer, M. Šob, Stability and elasticity of metastable solid solutions and superlattices in the Mo–Ta–N system: first-principles calculations, *Mater. Des.* 144 (2018) 310–322, <https://doi.org/10.1016/j.matdes.2018.02.033>.
- [39] S.F. Pugh, XCII. Relations between the elastic moduli and the plastic properties of polycrystalline pure metals, *London, Edinburgh, Dublin Philos. Mag. J. Sci.* 45 (1954) 823–843, <https://doi.org/10.1080/14786440808520496>.
- [40] D.G. Pettifor, Theoretical predictions of structure and related properties of intermetallics, *Mater. Sci. Technol.* 8 (1992) 345–349, <https://doi.org/10.1179/mst.1992.8.4.345>.
- [41] G.N. Greaves, A.L. Greer, R.S. Lakes, T. Rouxel, Poisson's ratio and modern materials, *Nat. Mater.* 10 (2011) 823–837, <https://doi.org/10.1038/nmat3134>.
- [42] V. Schnabel, B.N. Jaya, M. Köhler, D. Music, C. Kirchlechner, G. Dehm, D. Raabe, J.M. Schneider, Electronic hybridisation implications for the damage-tolerance of thin film metallic glasses, *Sci. Rep.* 6 (2016) 36556, <https://doi.org/10.1038/srep36556>.
- [43] N. Koutná, D. Holec, O. Svoboda, F.F. Klimashin, P.H. Mayrhofer, Point defects stabilise cubic Mo–N and Ta–N, *J. Phys. D Appl. Phys.* 49 (2016) 375303, <https://doi.org/10.1088/0022-3727/49/37/375303>.
- [44] G. Abadias, E. Chason, J. Keckes, M. Sebastiani, G.B. Thompson, E. Barthel, G.L. Doll, C.E. Murray, C.H. Stoessel, L. Martinu, Review Article: stress in thin films and coatings: current status, challenges, and prospects, *J. Vac. Sci. Technol. A Vacuum, Surfaces, Film.* 36 (2018) 020801, <https://doi.org/10.1116/1.5011790>.
- [45] P.C. Yashar, W.D. Sproul, Nanometer scale multilayered hard coatings, *Vacuum* 55 (1999) 179–190, [https://doi.org/10.1016/S0042-207X\(99\)00148-7](https://doi.org/10.1016/S0042-207X(99)00148-7).
- [46] M. Bartosik, R. Hahn, Z.L. Zhang, I. Ivanov, M. Arndt, P. Polcik, P.H. Mayrhofer, Fracture toughness of Ti–Si–N thin films, *Int. J. Refract. Metals Hard Mater.* 72 (2018) 78–82, <https://doi.org/10.1016/j.ijrmhm.2017.12.015>.
- [47] M. Bartosik, C. Rumeau, R. Hahn, Z.L. Zhang, P.H. Mayrhofer, Fracture toughness and structural evolution in the TiAlN system upon annealing, *Sci. Rep.* 7 (2017) 16476, <https://doi.org/10.1038/s41598-017-16751-1>.
- [48] W.M. Seidl, M. Bartosik, S. Kolozsvári, H. Bolvardi, P.H. Mayrhofer, Influence of Ta on the fracture toughness of arc evaporated Ti–Al–N, *Vacuum* 150 (2018) 24–28, <https://doi.org/10.1016/j.vacuum.2018.01.028>.
- [49] O. Kolednik, J. Predan, F.D. Fischer, P. Fratzl, Bioinspired design criteria for damage-resistant materials with periodically varying microstructure, *Adv. Funct. Mater.* 21 (2011) 3634–3641, <https://doi.org/10.1002/adfm.201100443>.
- [50] D.G. Sangiovanni, L. Hultman, V. Chirita, I. Petrov, J.E. Greene, Effects of phase stability, lattice ordering, and electron density on plastic deformation in cubic TiWN pseudobinary transition-metal nitride alloys, *Acta Mater.* 103 (2016) 823–835, <https://doi.org/10.1016/j.actamat.2015.10.039>.
- [51] G.R. Irwin, J.M. Kraft, P.C. Paris, A.A. Wells, Basic Aspects of Crack Growth and Fracture, Washington, D.C., 1967. <https://apps.dtic.mil/dtic/tr/fulltext/u2/663882.pdf>.
- [52] F.H. Mei, N. Shao, J.W. Dai, G.Y. Li, Coherent growth and superhardness effect of AlN/TiN nanomultilayers, *Mater. Lett.* 58 (2004) 3477–3480, <https://doi.org/10.1016/j.matlet.2004.07.005>.
- [53] V. Chawla, D. Holec, P.H. Mayrhofer, The effect of interlayer composition and thickness on the stabilization of cubic AlN in AlN/Ti–Al–N superlattices, *Thin Solid Films* 565 (2014) 94–100, <https://doi.org/10.1016/j.tsf.2014.06.051>.
- [54] J. Lin, J.J. Moore, B. Mishra, M. Pinkas, X. Zhang, W.D. Sproul, CrN/AlN superlattice coatings synthesized by pulsed closed field unbalanced magnetron sputtering with different CrN layer thicknesses, *Thin Solid Films* 517 (2009) 5798–5804, <https://doi.org/10.1016/j.tsf.2009.02.136>.
- [55] N. Koutná, P. Reháč, Z. Chen, M. Bartosik, M. Fallmann, M. Černý, Z. Zhang, M. Friák, M. Šob, P.H. Mayrhofer, D. Holec, Correlating structural and mechanical properties of AlN/TiN superlattice films, *Scripta Mater.* 165 (2019) 159–163, <https://doi.org/10.1016/j.scriptamat.2019.02.021>.
- [56] Z. Chen, D. Holec, M. Bartosik, P.H. Mayrhofer, Z. Zhang, Crystallographic orientation dependent maximum layer thickness of cubic AlN in CrN/AlN multilayers, *Acta Mater.* 168 (2019) 190–202, <https://doi.org/10.1016/j.actamat.2019.02.004>.
- [57] M. Bielawski, K. Chen, Computational evaluation of adhesion and mechanical properties of nanolayered erosion-resistant coatings for gas turbines, *J. Eng. Gas Turbines Power* 133 (2011) 042102, <https://doi.org/10.1115/1.4002158>.